

Displacement and Stress Monitoring of a Chemical Tanker Based on Inverse Finite Element Method

Adnan Kefal*, Erkan Oterkus**

* Department of Naval Architecture, Ocean and Marine Engineering University of Strathclyde
100 Montrose Street Glasgow G4 0LZ, United Kingdom

Phone: +44 (0)141 5484094

Fax: +44 (0)141 5522879

e-mail: adnan.kefal@strath.ac.uk

** Department of Naval Architecture, Ocean and Marine Engineering University of Strathclyde
100 Montrose Street Glasgow G4 0LZ, United Kingdom

Phone: +44 (0)141 5483876

Fax: +44 (0)141 5522879

e-mail: erkan.oterkus@strath.ac.uk

Abstract: Real-time reconstruction of full field structural displacements, strains, and stresses by using surface strain measurements obtained from on-board strain sensors is commonly referred to as shape- and stress-sensing. For this purpose, a computationally accurate, robust, and rapid algorithm named as inverse Finite Element Method (iFEM) was recently developed. The main goal of this study is to perform displacement and stress monitoring of a typical chemical tanker mid-ship based on iFEM methodology. The numerical implementation of the iFEM algorithm is done by considering four-node inverse quadrilateral shell (iQS4) element. In order to demonstrate the capability of the current approach, a long barge that has a cross-section identical to a typical chemical tanker is modelled with iQS4 elements. Then, hydrodynamic loads of the barge for a certain frequency of waves are calculated by using in-house hydrodynamic software. Then, these forces are applied to a FEM model of barge and structural response is computed by using in-house finite element software. The results obtained from FEM analysis is utilized as a source to simulate in-situ strain data used in iFEM analysis as input. Finally, iFEM and FEM displacements are compared and the effects of locations and number of sensors on iFEM solution accuracy are discussed.

Keywords: Shape Sensing; Stress Sensing; Inverse Finite Element Method; Chemical Tanker.

1. Introduction

A catastrophic failure and sinking of ships result in crucial financial losses, human life losses, and pollution of marine environment. Harsh marine environment together with strong weather conditions are very likely to cause structural damages on ship structures because ships are exposed to long-term cyclic loadings coming from continuous sea waves as well as short-term extreme loadings such as rogue waves, rainstorms, strong gales, seaquakes etc. Moreover, contact between sea water and material of ships (high strength steel in most cases) causes fast corrosion, erosion and hence thickness reduction. This phenomenon triggers initiation of damage growth and increases the size of an existing damage. Hence, a catastrophic failure of ships might be unavoidable, unless an appropriate on-site assessment of structural integrity is accomplished. Structural Health Monitoring (SHM) is a multidisciplinary technology area that addresses these problems through providing reliable real-time information from a structure about its global or local structural condition by integration of sensing systems on the structure. In other words, prevention of aforementioned serious damage cases and detailed structural management including inspection and maintenance plans can be achieved by performing an accurate SHM.

Dynamically tracking the three dimensional displacement and stress fields of a structure by utilizing a network of in-situ strain sensors and measured strains, generally known as shape- and stress-sensing, is a fundamental technology for SHM procedure. Since SHM systems potentially allow marine industry to increase both human and environmental safety in conjunction with reduction of maintenance costs, different monitoring schemes have been used for numerous years on different types of vessels. A typical hull structure monitoring system configuration for bulk carrier or tanker is proposed by LR (2004). The requirements that hull monitoring systems must meet are regulated by class societies such as ABS (1995) and DNV (2011). These rules specify the configuration and types of sensors to be used, as well as measurement accuracy, data storage and data analysis. However, these guidelines provide only a global outline on how data processing should take place and there has been little change in this basic configuration since IMO originally introduced requirements in 1994.

Apart from regulations defined by several class societies and IMO regarding hull structural monitoring, SHM of ships is considered as an important area of study by many researchers. Phelps and Morris (2013) provided a general review of the technical aspects of available hull structural monitoring systems with consideration of the differences between installations on navy ships as compared to commercial ships. Van der Cammen (2008) indicated hull structural monitoring systems that may be used for the assessment of motions and extreme events such as slamming stress and fatigue. Torkildsen (2005) stated an outline of a ship hull health monitoring installed on the Royal Norwegian. Their existing SHM system consists of a network of fibre-optic sensors to measure strain and temperature, X-band wave radar to estimate wave height and direction measurements, and a microwave altimeter mounted in the bow to measure the oncoming wave profile. Andersson et al. (2011) proposed a hull condition monitoring system for damage monitoring of ships which are made of fibre reinforced plastics. Their technique uses acoustic vibrations that exist in the hull structure and on-board sensors data as input. When a sensor is close to a damaged part of the hull, specific indications will be detected by the damage indication algorithm. Sielski (2012) experimentally monitored fatigue crack initiation and propagation of aluminium ship structures by using a ship structural reliability program including a SHM tool as a part. Their global method requires modal analysis and local method is dependent on the relation between lamb wave propagation and sensor diagnostics. Zhu and Frangopol (2013) used SHM data obtained from sensors to improve the accuracy and redundancy of reliability assessment of the ship cross-sections. Prior load effects are updated according to SHM data related to the wave-induced load by using Bayesian updating method. This study concluded that integration of the SHM data can considerably decrease the uncertainty in a distribution parameter, and hence updated performance indicators come closer to correct values. Hageman et al. (2013) developed a hull fatigue monitoring system for Floating Production Storage and Offloading (FPSO) vessels. Their fatigue prediction technique was developed based on Bayesian Statistics. Also, their system assesses the fatigue consumption from environmental conditions and measured strains separately, and compares with design fatigue consumption in order to define conclusions on performance of hull structure. Majewska et al. (2014) presented an experimental approach for SHM of sailing ships by using Fibre Bragg Grating (FBG) sensors. They installed FBG sensors grid to the foremast of a sailing ship in order to determine the strain/stress level of the foremast during different ship operations. Nichols et al.

(2014) described the structured decision making (SDM) process for using available information (loading data, model output, etc.) and producing a plan of action for maintaining the structure. Their example shows that SDM minimizes both transit time and probability of failure through a user-defined cost function. However, developing this approach requires models that describe the loading data, predict the structural response to the load, and forecast accumulated damage.

Most of the aforementioned SHM approaches don't take into account the advanced structural topologies and boundary conditions. Moreover, they mostly require sufficiently accurate loading information even though it is not easy to estimate dynamic loads of waves and winds due to the complexity and statistical feature of oceanographic phenomena. Furthermore, some of them are not appropriate for use in real-time due to the time-consuming analysis. A novel shape- and stress-sensing algorithm named as inverse Finite Element Method (iFEM) was developed by Tessler and Spangler (2003, 2005) at NASA Langley Research Centre. iFEM algorithm reconstructs the structural deformations, strains and stresses by utilizing the strain data obtained from a network of on-board strain sensors located at various sites of a structure. iFEM methodology is based upon the minimization of a weighted-least-square functional. In other words, the formulation involves the entire structural geometry that is discretized by using suitable inverse finite elements in which the measured strain data are adapted to the element strains in a least-square sense. Unlike other developed SHM methods, iFEM methodology possesses a general applicability to complex structures subjected to complicated boundary conditions in real-time (Tessler and Spangler 2005). Since only on-board strain measurements are used as input to the iFEM formulation, accurate structural deformed shapes of engineering structures that are under any type of static and/or dynamic loadings can be obtained without prior knowledge of material properties. Once the structural deformed shape is reconstructed, the full field strains can be calculated by utilizing the displacements. Then, the three-dimensional stress state of the structure can be evaluated from the full field strains and the material properties of the structure. Finally, three-dimensional stresses can be adapted to an equivalent stress by means of an appropriate failure criterion which can enable real-time damage prediction.

iFEM framework has already shown to be precise, powerful and sufficiently fast for real-time applications (Gherlone et al. 2012, 2014). iFEM formulation is applicable to monitor thin and moderately thick beam, plate and shell structures because inverse beam, frame, or plate and shell

finite elements can be simply used for discretization of the physical domain. Cerracchio et al. (2010) and Gherlone et al. (2011, 2012, 2014) developed a robust inverse-frame finite element by adopting kinematic assumptions of Timoshenko beam theory including stretching, bending, transverse shear and torsion deformation modes. The capability of their inverse-frame element is numerically and experimentally verified for shape-sensing of three-dimensional frame structures undergoing static and/or damped harmonic excitations. Furthermore, Tessler and Spangler (2003, 2004) focused on the inverse problem of reconstructing the three-dimensional displacements in plate and shell structures from strain sensor measurements. Based upon first-order shear deformation theory, Tessler and Spangler (2004) developed a three-node inverse shell element (iMIN3) by using lowest-order anisoparametric C^0 – continuous functions, i.e., linear in-plane displacements and bending rotations, and a constrained type quadratic deflection. The precision of iMIN3 element was also confirmed by using experimentally measured-strain data (Quach et al. 2005, Vazquez et al. 2005). Moreover, Tessler et al. (2012) recently improved iMIN3 element formulation to reconstruct deformed shape of plate and shell structures undergoing large displacements. Furthermore, Cerracchio et al. (2013, 2015) enhanced the Tessler and Spangler (2003, 2005) iFEM formulation for shape- and stress-sensing of multi-layered composite and sandwich structures. They reformulated the original plate/shell iFEM formulation to include the kinematic assumptions of recently developed Refined Zigzag Theory by Tessler et al. (2009, 2010). However, all proposed iFEM formulations as a numerical or experimental application on engineering structures have been limited to the SHM of aerospace vehicles (Tessler et al. 2011, Gherlone et al. 2013).

The main and novel aim of this work is to apply iFEM methodology for shape- and stress-sensing of a chemical tanker for the first time in the literature. First, a four-node inverse quadrilateral shell (iQS4) element formulation is presented under the assumptions of Mindlin's first-order plate theory. Then, as a practical application to marine structures, a long barge that has a cross-section similar to a typical chemical tanker is considered and analysed based on the presented iFEM algorithm. In order to make the application more realistic, a hydrodynamic model of the barge is performed by using the hull form (panels) as well as its wetted surface properties and wave properties such as height, angle, and frequency as input. As an output, hydrodynamic ship loading and rigid body motion of the barge are obtained. Then, finite element analysis of the model is performed by using the loading calculated from hydrodynamic analysis.

The strain output of finite element model is used to represent the ‘experimental’ strain measurements (i.e., in-situ strain data or simulated sensor-strain). Finally, the iFEM model is performed for displacement and stress monitoring of the chemical tanker cross-section by utilizing the simulated strain data obtained from various locations of the structure. Finally, the effects of sensor positions and number of sensors on iFEM solution accuracy are discussed.

2. Inverse finite element formulation for shells

2.1. Inverse quadrilateral shell element

A four-node inverse quadrilateral shell (iQS4) element is used to demonstrate the iFEM formulation. In order to define the local element functions, a local coordinate system xyz is located with reference to iQS4 element and global Cartesian coordinate system XYZ as shown in Figure 1a. The iQS4 element has six degrees-of-freedom (DOF) per node, as shown in Figure 1b, and they consist of translations u_i , v_i , and, w_i as well as rotations θ_{xi} , θ_{yi} , and θ_{zi} .

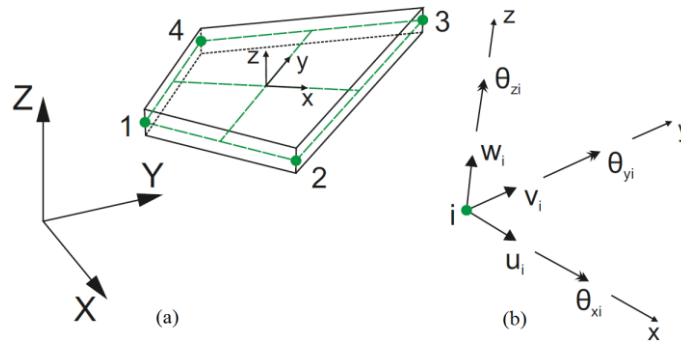


Figure 1 (a) iQS4 element showing global and local coordinate systems. (b) Nodal DOF in the local coordinate system xyz .

The origin of xyz system is positioned at the centroid of element’s mid-plane quadrilateral along uniform shell thickness $z \in [-t, +t]$. When assembling the elements, transformation of nodal DOF from the local to global coordinate system can easily be done by utilizing global XYZ coordinates of nodes. The iQS4 element formulation is derived by first writing membrane and

bending stiffness matrices separately and finally adding them together. This procedure is a common and sufficiently accurate way to obtain the element formulation. Three components of the displacement vector of the element are described according to the assumptions of Mindlin's first-order plate theory. The strain–displacement relations of linear elasticity theory are derived by calculating the relevant derivatives of the three components of the displacement vector. For brevity, these relations can be written in compact vector forms by utilizing nodal displacement vector of iQS4 element \mathbf{u}^e and derivatives of shape functions \mathbf{B}^m , \mathbf{B}^k , \mathbf{B}^s as

$$\begin{Bmatrix} \varepsilon_{xx} \\ \varepsilon_{yy} \\ \gamma_{xy} \end{Bmatrix} \equiv \mathbf{e}(\mathbf{u}^e) + z\mathbf{k}(\mathbf{u}^e) = \mathbf{B}^m\mathbf{u}^e + z\mathbf{B}^k\mathbf{u}^e \quad (1a)$$

and

$$\begin{Bmatrix} \gamma_{xz} \\ \gamma_{yz} \end{Bmatrix} \equiv \mathbf{g}(\mathbf{u}^e) = \mathbf{B}^s\mathbf{u}^e \quad (1b)$$

where

$$\mathbf{u}^e = [\mathbf{u}_1^e \quad \mathbf{u}_2^e \quad \mathbf{u}_3^e \quad \mathbf{u}_4^e]^T \quad (1c)$$

and

$$\mathbf{u}_i^e = [u_i \quad v_i \quad w_i \quad \theta_{xi} \quad \theta_{yi} \quad \theta_{zi}]^T \text{ with } (i=1,2,3,4) \quad (1d)$$

The interpolation functions (or shape functions) used to describe membrane, bending curvatures, and transverse shear actions of iQS4 element are analogous to four-node flat shell element described by Cook (1994) and MIN4 (Mindlin-type, four-nodes) element provided by Tessler and Hughes (1983). Herein, shape functions of the deflection variables are derived from biquadratic serendipity interpolation, whereas the normal rotations are interpolated by using standard bilinear functions. Using these interpolation functions for the kinematic field of the iQS4 element leads to C^0 continuity, thus ensuring the element interior and edge interface continuities.

The membrane strains $\mathbf{e}(\mathbf{u}^e)$ are associated with the stretching of the middle surface. Therefore, \mathbf{B}^m matrix stands for the derivatives of the shape functions associated with the

membrane behaviour. Furthermore, $\mathbf{k}(\mathbf{u}^e)$ and $\mathbf{g}(\mathbf{u}^e)$ are the bending curvatures and the transverse shear strains, respectively. Hence, \mathbf{B}^k and \mathbf{B}^s matrices are the corresponding derivatives of shape functions used to define bending behaviour of the element. The explicit forms of the \mathbf{B}^m , \mathbf{B}^k , and \mathbf{B}^s matrices as well as the interpolation functions of iQS4 element are given in Appendix A. It is important to mention that ε_{zz} has no role in the internal work due to the plane stress assumption $\sigma_{zz} = 0$.

2.2. Input data from in-situ strain sensors

Discrete in-situ strain measures obtained from the sensors placed on-board structure are fundamental input of the iFEM methodology. Conventional strain rosettes or embedded fiber-optic sensor networks including Fibre Bragg Grating (FBG) sensors and Sensing Fiber Optic Cables are promising technology to collect large amount of on-board strain data. Fibre-optic systems potentially offer a number of advantages for marine structure installations as they are lightweight, high speed, and not affected by electromagnetic interference and they require no re-calibration once installed. Figure 2 illustrates the positions of the in-situ strain rosettes on an iQS4 element's surfaces for computing the reference plane strains and curvatures.

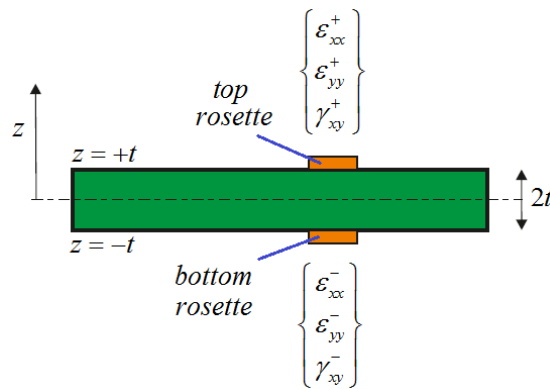


Figure 2 Discrete surface strains measured at location \mathbf{x}_i from strain rosettes instrumented on top and bottom of iQS4 elements.

Tessler and Spangler (2005) indicated that the reference plane strains \mathbf{e}_i^ε and curvatures \mathbf{k}_i^ε can be calculated by using the surface strains measured at n discrete locations ($\mathbf{x}_i = x_i, y_i, \pm t$) ($i = 1, \dots, n$) as

$$\mathbf{e}_i^\varepsilon = \frac{1}{2} \begin{Bmatrix} \varepsilon_{xx}^+ + \varepsilon_{xx}^- \\ \varepsilon_{yy}^+ + \varepsilon_{yy}^- \\ \gamma_{xy}^+ + \gamma_{xy}^- \end{Bmatrix}_i \text{ with } (i = 1, n) \quad (2a)$$

$$\mathbf{k}_i^\varepsilon = \frac{1}{2t} \begin{Bmatrix} \varepsilon_{xx}^+ - \varepsilon_{xx}^- \\ \varepsilon_{yy}^+ - \varepsilon_{yy}^- \\ \gamma_{xy}^+ - \gamma_{xy}^- \end{Bmatrix}_i \text{ with } (i = 1, n) \quad (2b)$$

In Eqs. (2), the measured surface strains are denoted as $(\varepsilon_{xx}^+, \varepsilon_{yy}^+, \gamma_{xy}^+)_i$ and $(\varepsilon_{xx}^-, \varepsilon_{yy}^-, \gamma_{xy}^-)_i$ where superscripts ‘+’ and ‘-’ represent the top and bottom surface locations, and the following notation is used $(\bullet)_i = (\bullet)_{\mathbf{x}=\mathbf{x}_i}$. In fact, the reference plane strains \mathbf{e}_i^ε and curvatures \mathbf{k}_i^ε are associated with the membrane strains $\mathbf{e}(\mathbf{u}^e)$ and bending curvatures $\mathbf{k}(\mathbf{u}^e)$ described in Eq. (1a). In the deformation of thin shells, contributions of \mathbf{g}_i^ε are much smaller compared to the bending curvatures \mathbf{k}_i^ε . Since most of the marine structures are suitable to be modelled by using thin shells, the \mathbf{g}_i^ε contributions can be safely omitted.

2.3. Weighted least-squares functional of inverse finite element method

By taking into account the membrane, bending and transverse shear deformations of the individual element, the inverse finite element method reconstructs the deformed shape by minimizing an element functional, namely a weighted least-squares functional $\Phi_e(\mathbf{u}^e)$

$$\Phi_e(\mathbf{u}^e) = w_e \|\mathbf{e}(\mathbf{u}^e) - \mathbf{e}^\varepsilon\|^2 + w_k \|\mathbf{k}(\mathbf{u}^e) - \mathbf{k}^\varepsilon\|^2 + w_g \|\mathbf{g}(\mathbf{u}^e) - \mathbf{g}^\varepsilon\|^2 \quad (3a)$$

with respect to the unknown displacement DOF (Tessler and Spangler 2005). The squared norms expressed in Eq. (3a) can be written in the form of the normalized Euclidean norms as

$$\|\mathbf{e}(\mathbf{u}^e) - \mathbf{e}^\varepsilon\|^2 = \frac{1}{n} \iint_{A^e} \sum_{i=1}^n (\mathbf{e}(\mathbf{u}^e)_i - \mathbf{e}_i^\varepsilon)^2 dx dy \quad (3b)$$

$$\|\mathbf{k}(\mathbf{u}^e) - \mathbf{k}^\varepsilon\|^2 = \frac{(2t)^2}{n} \iint_{A^e} \sum_{i=1}^n (\mathbf{k}(\mathbf{u}^e)_i - \mathbf{k}_i^\varepsilon)^2 dx dy \quad (3c)$$

$$\|\mathbf{g}(\mathbf{u}^e) - \mathbf{g}^\varepsilon\|^2 = \frac{1}{n} \iint_{A^e} \sum_{i=1}^n (\mathbf{g}(\mathbf{u}^e)_i - \mathbf{g}_i^\varepsilon)^2 dx dy \quad (3d)$$

where A^e represents the area of the element. During the implementation of the iQS4 element, all the integrations given in Eqs. (3b-3d) are carried out via four-point Gaussian quadrature for a constant thickness element. The weighting constants w_e , w_k , and w_g in Eq. (3a) are positive valued and stand for individual section strains. They control the complete coherence between theoretical strain components and their experimentally measured values.

If all in-situ strains \mathbf{e}_i^ε , \mathbf{k}_i^ε , and \mathbf{g}_i^ε are known by utilizing the measured surface strains collected from on-board strain sensors, the weighting constants are $w_e = w_k = w_g = 1$ for the squared norms given in Eqs. (3b-3d). However, for any case of missing in-situ strain component, the corresponding weighting constants can be adjusted to a small positive coefficient such as $\alpha = 10^{-4}$ (Tessler et al., 2011). Moreover, for thin shells, the weighting constant w_g can be set as $w_g = \alpha = 10^{-4}$, whereas the remaining weighting constants can be specified as $w_e = w_k = 1$ because the displacements due to the transverse shear strains \mathbf{g}_i^ε are much smaller compared to bending curvatures \mathbf{k}_i^ε . This adjustment of weighting constants ensures satisfactory regularization of Eq. (3a) and provides accurate solutions for thin shells.

If none of the aforementioned strain sensors is placed to an inverse element, the element is missing all of the in-situ strain components \mathbf{e}_i^ε , \mathbf{k}_i^ε , and \mathbf{g}_i^ε , so it is called ‘strainless inverse element’. In order to ensure the satisfactory regularization of iFEM model, all of the weighting coefficients should be adjusted to a small positive coefficient $w_e = w_k = w_g = \alpha = 10^{-4}$ for a strainless inverse element. Hence, the necessary interpolation functional connectivity can be established between the elements that have strain-sensor data, even if the iFEM model has very sparse measured strain data. Note that increasing the number of strainless inverse elements may decrease the accuracy of the solution.

By virtue of these assumptions, all strain compatibility relations are explicitly satisfied so that Eq. (3a) can be minimized with respect to nodal displacement vector as

$$\frac{\partial \Phi_e(\mathbf{u}^e)}{\partial \mathbf{u}^e} = \mathbf{k}^e \mathbf{u}^e - \mathbf{f}^e = 0 \quad (4a)$$

After the minimization, the resulting element matrix equation is obtained as

$$\mathbf{k}^e \mathbf{u}^e = \mathbf{f}^e \quad (4b)$$

where \mathbf{k}^e is the element left-hand-side matrix, \mathbf{f}^e is the element right-hand-side vector that is a function of the measured strain values, and \mathbf{u}^e is the nodal displacement vector of the element. Once the local matrix equations are defined, the element contributions to the global linear equation system of the discretized structure can be obtained as

$$\mathbf{K}\mathbf{U} = \mathbf{F} \quad (4c)$$

where \mathbf{K} is independent of the measured strain values, \mathbf{U} is the global nodal displacement vector, and \mathbf{F} is the global function of the measured strain values. Although the global left-hand-side matrix \mathbf{K} includes the rigid body motion mode of the discretized structure, it can be reduced to a positive definite matrix by prescribing problem-specific displacement constraints. Since \mathbf{K} remains unchanged for a given distribution of strain sensors, it needs to be inverted only once during monitoring process. As a result, solution of this equation system can be done very rapidly. On the other hand, the right-hand-side vector \mathbf{F} needs to be updated during the monitoring process because it is dependent on the discrete surface strain data obtained from in-situ strain sensors. Finally, the matrix–vector multiplication $\mathbf{K}^{-1}\mathbf{F}$ gives rise to the unknown DOF vector \mathbf{U} , which provides the deformed structural shape at any real-time.

Once the primary unknowns, namely nodal displacements, are calculated at any real-time, the strains at any point in an iQS4 element can also be calculated at any real-time by using the derivatives of shape functions. After determining the real-time strains, real-time stresses can be obtained by using constitutive equations. Bhatti (2006) described direct finite element method stress calculations and proposed several techniques including interpolation-extrapolation of stresses, and average nodal stresses in order to calculate element stresses more precisely. Since

the presented iFEM formulation inherits standard displacement-based formulation, the stress calculation methods proposed by Bhatti (2006) can be directly followed.

3. iFEM analysis of a chemical tanker cross-section

A typical chemical tanker cross-section as well as its structural components is presented in Figure 3 (Dokkum, 2003). A long barge that has a very similar cross-section to this typical chemical tanker is designed and modelled with iQS4 elements in order to demonstrate the robustness and practicality aspects of iFEM methodology for performing an accurate shape- and stress-sensing operation. Isometric view of the barge cross-section and detailed dimensions of its structural components are included in Appendix B.

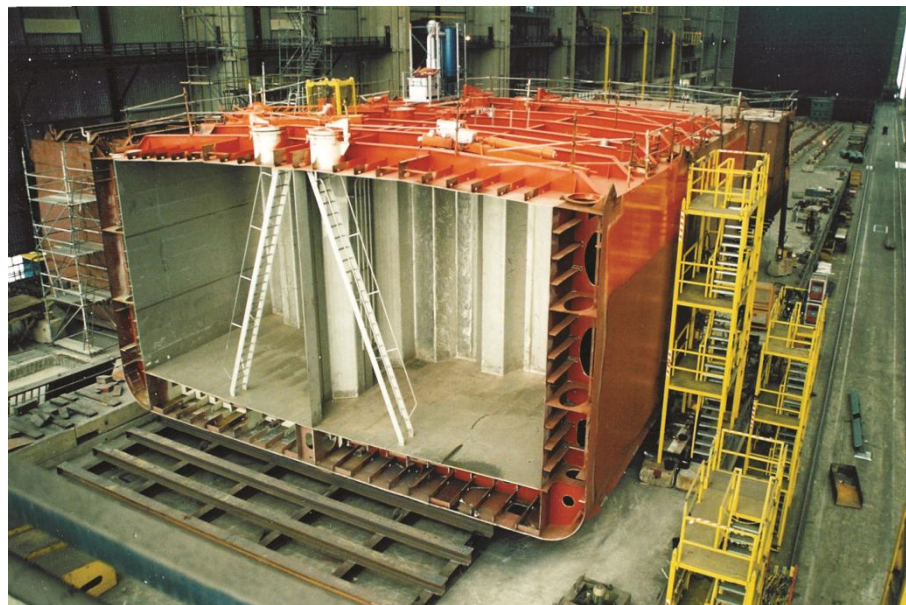


Figure 3 View of a tank inside a typical chemical tanker (Dokkum, 2003)

For simplicity, it is desirable to define only one axis system and the defined global Cartesian coordinate system has its origin on the still water plane aligned vertically with the ship's centre of gravity. The x-y plane is coincident with the calm water level where x-axis is along the main direction of the ship, the y-axis points at the port side of the ship, and z-axis is positive upwards

i.e. in the opposite direction of gravity. According to the defined Cartesian coordinate system, main particulars of the barge are listed in Table 1.

Table 1 Main particulars of barge

Particular	Value	Unit
Length (over all)	100	m
Breadth (moulded)	20	m
Depth (moulded)	10.5	m
Designed load draft (moulded)	8.25	m
Block coefficient (at designed draft)	0.997	m ³ /m ³
Displacement at designed draft	16861.5	tonnes
Deadweight at designed draft	14979	tonnes
Light ship weight	1882.5	tonnes
Vertical centre of buoyancy	-4.11	m
Vertical centre of gravity	-2.424	m
Vertical centre of deadweight	-2.25	m
Vertical centre of light ship	-3.81	m
Radius of gyration around x axis	7.458	m
Radius of gyration around y axis	29.253	m
Radius of gyration around z axis	29.433	m
Radius of gyration for roll-yaw product of inertia	0	m

It has been assumed that total number of cargo holds is eight, frame spacing between the transverse frames is 1.25 m, and all the structural components including plates, stiffeners, and bulkheads have the uniform thickness of 12 mm. All structural components of the barge are made of steel having elastic modulus of 210 GPa and Poisson's ratio of 0.3. In order to represent complexity of the structure more clearly, several isometric views of the barge structural model are included in Appendix B.

In this study, the solution is obtained by combining three different tools. First, a hydrodynamic analysis is performed to calculate the hydrodynamic forces. By using these forces as a loading condition, FEM analysis of the barge is performed to calculate the numerical strain data to be used as an input for the iFEM analysis. Finally, iFEM analysis is performed by simulated strain data obtained from direct FEM analysis.

The design of marine structures such as ships, offshore and coastal structures is significantly affected by wave-body dynamics. Therefore, hydrodynamic analysis of rigid bodies that are freely oscillating under the free water surface is extremely important. An in-house panel method code, which is a frequency-domain hydrodynamic software, is utilized to predict the motions and wave loads of the barge. The barge is assumed to move with zero forward speed in deep water at angle $\beta = 180^\circ$ to regular sinusoidal waves which describes the waves coming from ahead, namely head seas condition. Six DOF motions of the barge are calculated for a wave amplitude of 1 m and wave frequencies starting from 0.2 rad/s to 1.5 rad/s. Full hydrodynamic model of the barge is discretized by using 2508 flat quadrilateral panels as shown in Figure 4.

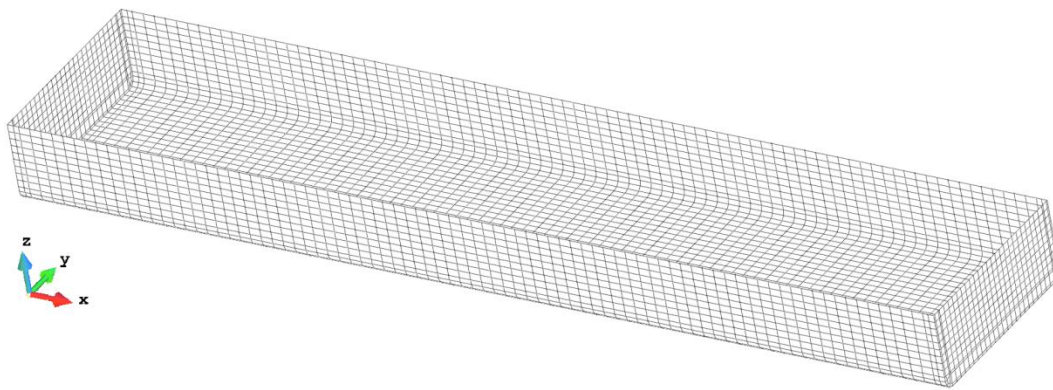


Figure 4 Full hydrodynamic model of the barge

The discretized body, namely coordinates of nodes used to generate the panels and nodal connectivity of these panels, is the main input for the in-house frequency-domain hydrodynamic software. The software first calculates radiation and diffraction source strengths and then velocity potentials at the centroids of the hydrodynamic panels for requested heading and frequency based on three dimensional potential flow theory and zero speed Green's function (Wehausen and Laitone, 1960; Beck and Loken, 1989; and Papanikolaou and Schellin, 1992). Since the barge floats in head seas condition, the in-house panel method code takes into account the advantage of the lateral symmetry condition (x - z plane symmetry) and generates the source strength results by using only 1254 panels. By utilizing the velocity potentials of radiated and diffracted waves, the software solves a complex form of linear and harmonic oscillatory rigid

body motion equation with respect to the barge centre of gravity and generates the six DOF motion results of the barge. The numerical sway, roll and yaw motion amplitudes with respect to barge centre of gravity are negligibly small and in fact these results are theoretically zero because the barge is affected by head sea waves only. The motion amplitudes with respect to the barge's centre of gravity for the remaining directions namely surge, heave, and pitch are illustrated in Figures 5.

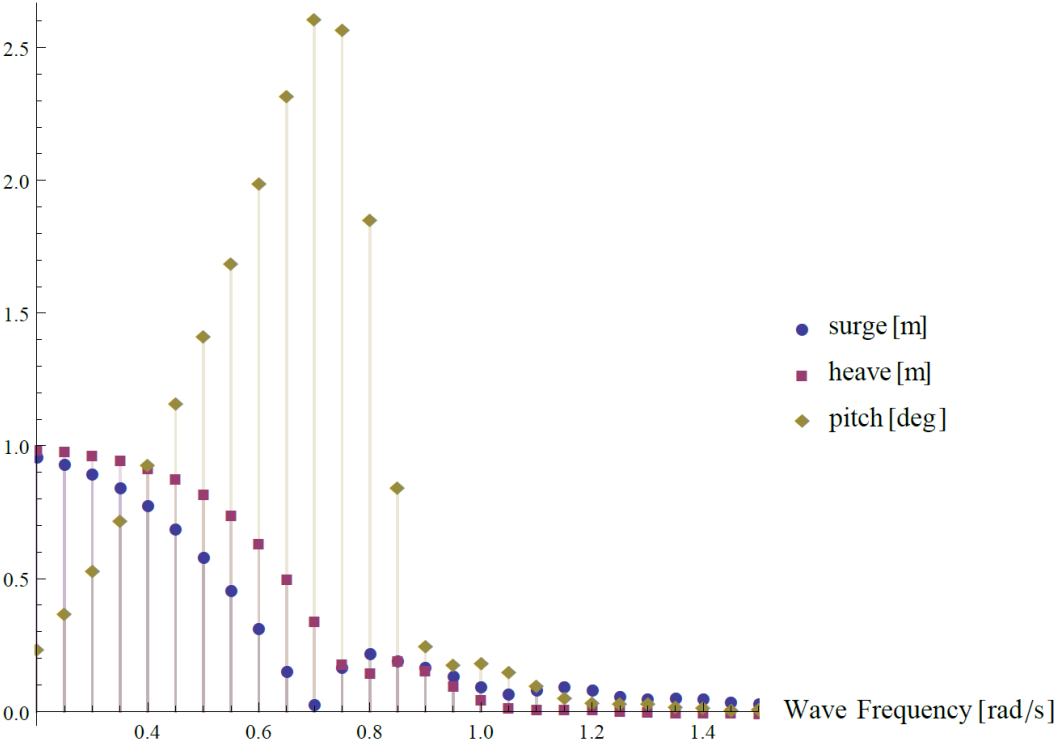


Figure 5 Barge's motion amplitudes with respect to wave frequencies [rad/s]

The change of the motion amplitudes in surge, heave and pitch directions is significant around the frequency value of 0.5 rad/s in terms of structural analysis because the oscillatory dynamic pressure calculated at this frequency causes the highest vertical bending moment distribution along the length of the barge. The hydrodynamic force variation along the barge underwater panels due to the oscillation at 0.5 rad/s is plotted in Figure 6.

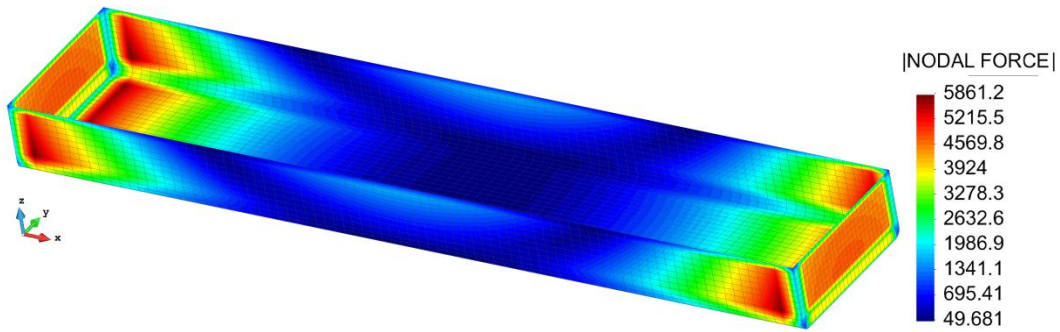


Figure 6 Barge's total hydrodynamic force [N] distribution for the frequency value of 0.5 rad/s

For a floating structure, it is important to obtain equilibrium before performing a direct FEM analysis because an imbalanced model causes an unrealistic result. Therefore, computed hydrodynamic forces and their corresponding inertia loads are applied to the direct FEM model of the structure in order to find a realistic global structural response of the barge. Application of inertia loads is done by associating the acceleration vector to each finite element while hydrodynamic forces are applied to the nodes of each finite element below still water. Barge geometry and its constraint conditions as well as loading conditions are symmetric with respect to both x-z and y-z plane. So, there is no need to perform direct FEM analysis of the entire structure. Hence, only one quarter of the barge is discretised by using 6908 nodes and 11065 elements as shown in Figure 7.

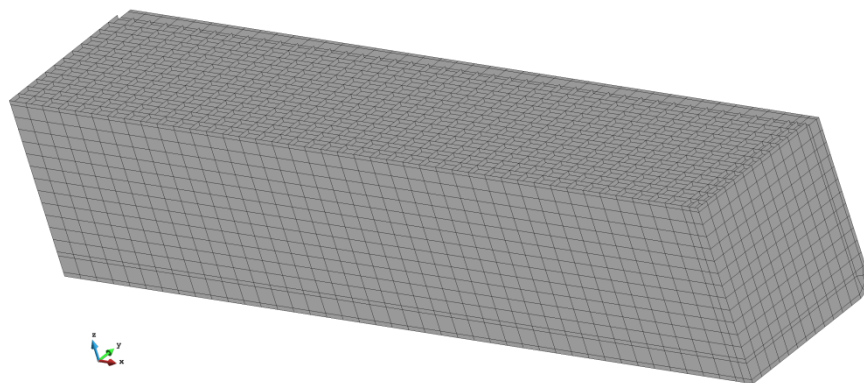


Figure 7 One quarter of the barge mesh

For the application of constraint conditions, translation along normal direction of symmetry plane and rotations around the symmetry plane axial directions are fixed for each symmetry plane. Moreover, the structural model is fixed by an artificial support along z-direction in order to disable the rigid body motion. After performing the FEM analysis, the reaction force calculated at this artificial support is checked to ensure that it doesn't affect the actual equilibrium of hydrodynamic pressures and inertia loads. The loading conditions are also applied by considering the symmetry planes. As mentioned earlier, the resulting total deflection and rotation obtained from direct FEM analysis are used to produce the simulated sensor-strain data.

4. Case studies for iFEM analysis

Three different case studies of the barge are considered based on iFEM methodology by using different number of strain rosettes and their altered locations. An iFEM model, which is composed of iQS4 elements and geometrically identical to the quarter mesh model used in direct FEM analysis (Figure 7), is adopted in the following iFEM analysis. The strain rosettes have to be placed at the top and bottom surfaces of the iQS4 elements whose resulting deformations exhibits both stretching and bending actions due to the complexity of the barge structure. However, for the iQS4 elements whose mid-planes are superimposed on the x-z and y-z symmetry planes of the barge, the strain rosettes are only located at the top surface of these elements. Since the material properties are symmetric with respect to mid-planes of these iQS4 elements and their resulting deformations are due to stretching only, the strain distributions are symmetric with respect to their mid-planes.

In the first case, all the iQS4 elements used in discretization of iFEM model are assumed to be installed with strain sensors in order to examine the results when one-to-one mapping of the relevant strain data from direct FEM to iFEM analysis is made. Therefore, the total number of iQS4 elements that are installed with strain rosettes is 11065 from which 688 and 236 of them belongs to the x-z and y-z symmetry planes of the barge, respectively. As mentioned earlier, the strain rosettes are placed at the centroids of the top surfaces of these 924 iQS4 elements, whereas the strain rosettes are positioned on the centroids of both the top and bottom surfaces of the remaining 10141 iQS4 elements. Thus, the total number of the strain rosettes is 21206. Since the

barge structure is constructed with thin shells, the weighting constants associated with the transverse shear strains are set as $w_g = 10^{-4}$, whereas the remaining weighting constants for membrane strains and bending curvatures are respectively set as $w_e = w_k = 1$. The total displacement results found in iFEM analysis are shown together with the reference FEM results in Figure 8.

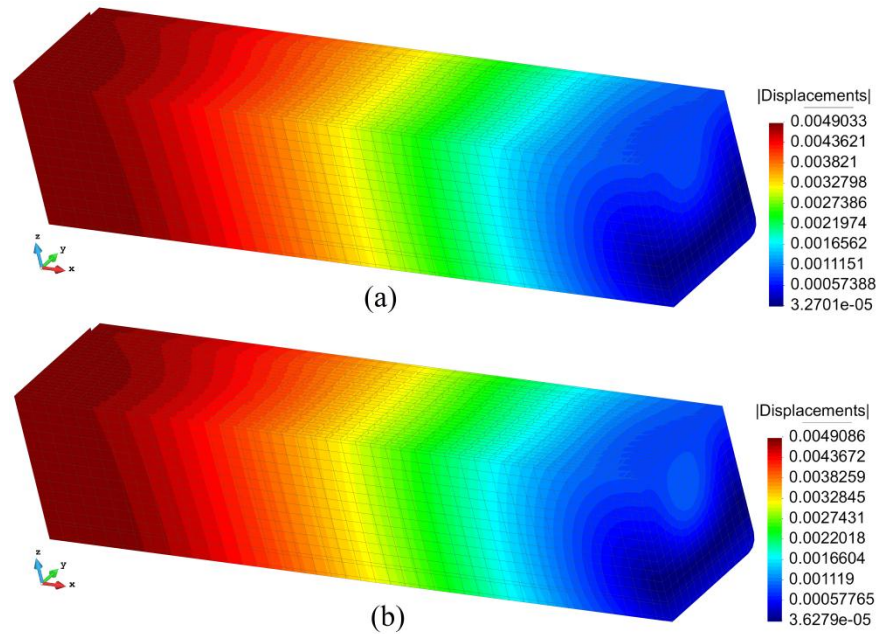


Figure 8 (a) iFEM total displacement [m] distribution for one-to-one strain data. (b) Direct finite element total displacement [m] distribution

According to the distributions, both maximum displacements are approximately 4.9 mm confirming that iFEM methodology can capture very promisingly expected results when all the structural components in one quarter of the barge are installed with strain sensors.

Once a full field deformed shape of the barge is obtained, full field three-dimensional stress state of the barge body can be calculated by using displacement results. Then, three-dimensional stresses can be converted into an equivalent stress by utilizing an appropriate failure criterion. The von Mises failure criterion is the most commonly used failure criterion for metals, thus full field von Mises stresses on the top surfaces of the shells are calculated in iFEM analysis and

compared with those found in direct FEM solution. Both von Mises stress distributions are plotted together in Figure 9 and contours of stress colours are identically matching each other. Moreover, the difference between the maximum von Mises results is 2.23% proving the superior accuracy of iFEM algorithm.

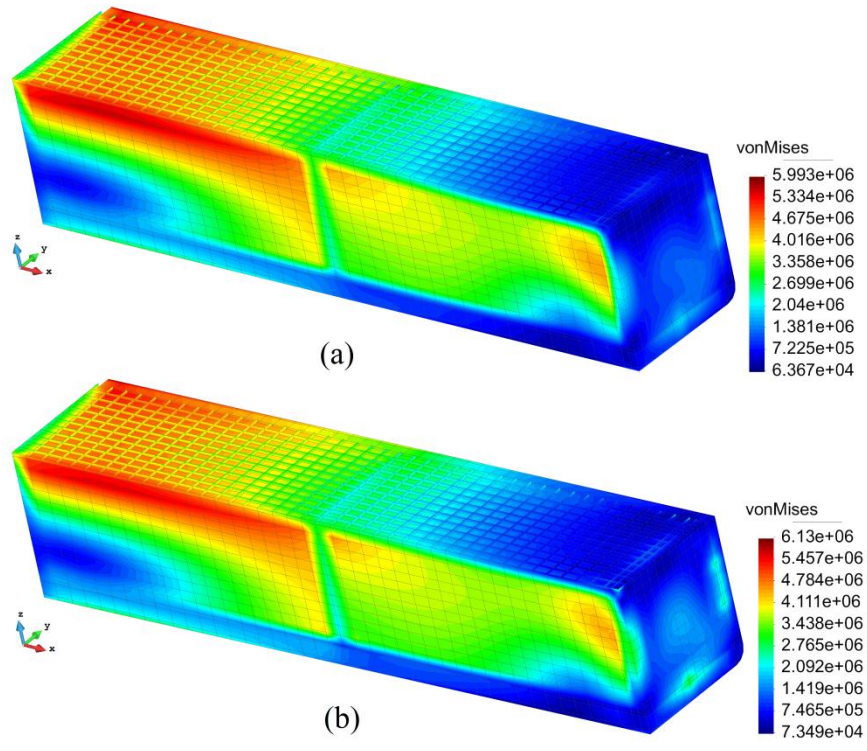


Figure 9 (a) iFEM von Mises stress [Pa] distribution for one-to-one strain data. (b) Direct finite element vonMises stress [Pa] distribution

Secondly, iFEM analysis of the barge is performed when all strain rosettes used in the first case study are removed except the ones glued on the central deck stiffener, the central longitudinal bulkhead, and the central girder. This case study is done to assess the precision of iFEM methodology when there are missing in-situ strain measurements. After removal of the strain rosettes, iFEM analysis of the barge is conducted by using the strain data collected from 688 iQS4 elements which are superimposed on the x-z symmetry plane of the barge. The strain rosettes are only positioned on the top surfaces' centroids of these 688 iQS4 elements. Therefore,

total number of strain rosettes is 688 for this case study. The exact locations of the strain rosettes are clearly illustrated in Figure 10.

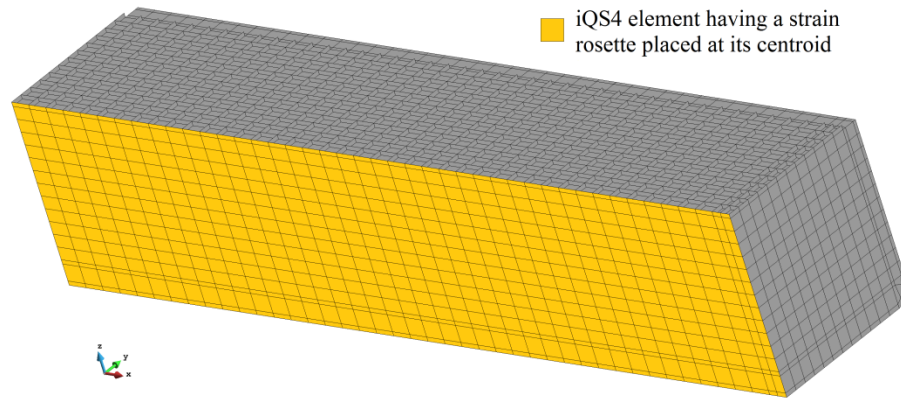


Figure 10 Exact locations of the strain rosettes on x-z symmetry plane

For iQS4 elements on which the strain data is available, the membrane strain's weighting constants and bending curvature's weighting constants are both set as $w_e = w_k = 1$, while their transverse shear strain's weighting constants are set as $w_g = 10^{-4}$. For iQS4 elements that do not have any sensors, namely strainless iQS4 elements, their weighting constants are set as $w_e = w_k = w_g = 10^{-4}$. In both iFEM and direct FEM analysis, the von Mises stresses are evaluated according to the top surfaces of the shells. The total displacements as well as the von Mises stresses obtained from iFEM analysis are respectively compared with direct FEM results as depicted in Figure 11-12.

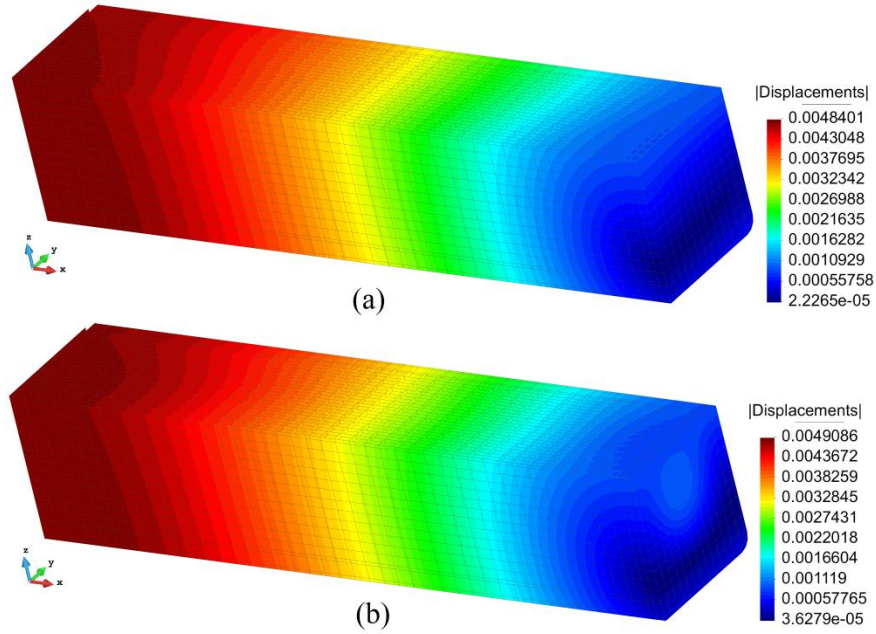


Figure 11 (a) iFEM total displacement [m] distribution for only strain data collected from x-z symmetry plane. (b) Direct finite element total displacement [m] distribution.

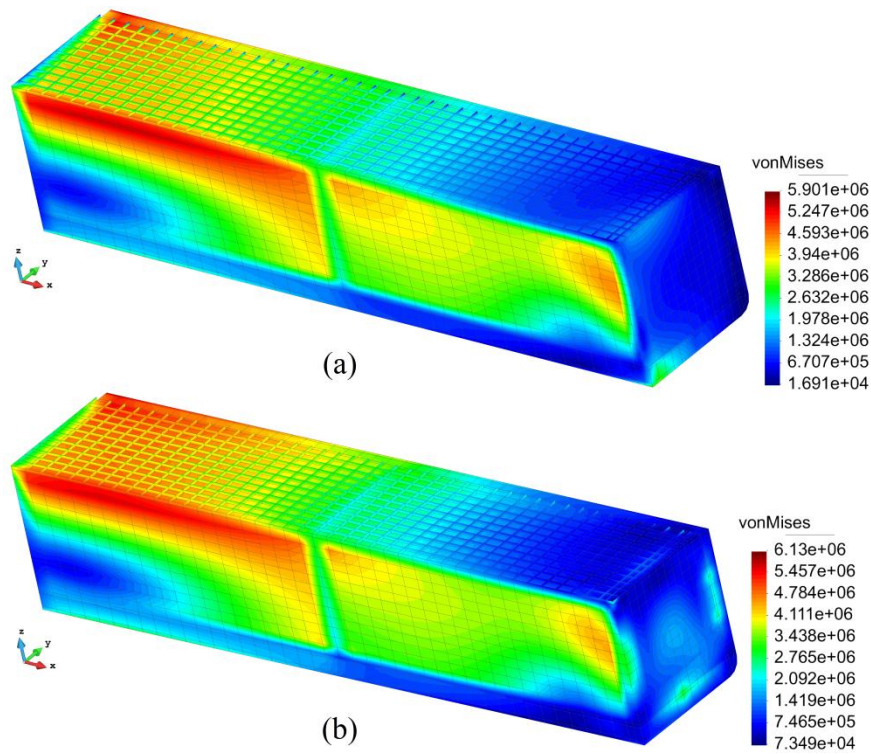


Figure 12 (a) iFEM von Mises stress [Pa] distribution for only strain data collected from x-z symmetry plane. (b) Direct finite element vonMises stress [Pa] distribution

The iFEM-reconstructed displacement and von Mises stress fields fairly agree with the reference displacement and von Mises stress results. The error between the maximum displacements is 1.41%, whereas the error is 3.74% for von Mises stress comparison. Hence, this accuracy confirms the robustness of iFEM framework even if there are missing in-situ strain measurements.

Although the results obtained in the first two case studies are completely satisfactory, the proposed number of strain rosettes may be high for a practical application. Therefore, in the third case study, the iFEM analysis of the barge is performed based on the same mesh, but only using the strain data obtained from strain rosettes located at the central deck stiffener, the central girder and several critical locations on the central longitudinal bulkhead including the neutral axis of the barge, the edge near to deck, and the edges near to the transverse bulkhead. This case study not only assesses the practical applicability, but also examines the precision of iFEM formulation according to the effect of sensor locations and number of sensors on solution accuracy. After eliminating majority of the strain sensors, the strain data collected from 196 iQS4 elements are used to perform shape- and stress-sensing of the barge. Similar to the second case study, each of these 196 iQS4 elements are installed with only one strain sensor on the centroid of the top surface because these inverse elements belong to x-z symmetry plane. Therefore, the total number of stain rosettes is decreased to 196 and the exact locations of these sensors are clearly presented in Figure 13.

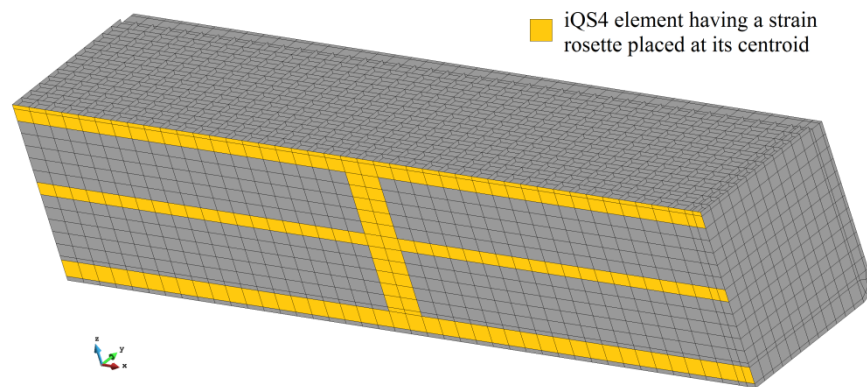


Figure 13 Exact locations of the strain rosettes on the central deck stiffener, the central girder, and the central longitudinal bulkhead

As in the second case study, the weighting coefficients are set to $w_e = w_k = w_g = 10^{-4}$ for each strainless iQS4 elements, whereas they are set to $w_e = w_k = 1$ and $w_g = 10^{-4}$ for each iQS4 element on which the strain sensors are located. The total displacements distributions obtained from iFEM analysis are consistent with direct FEM results as represented in Figure 14.

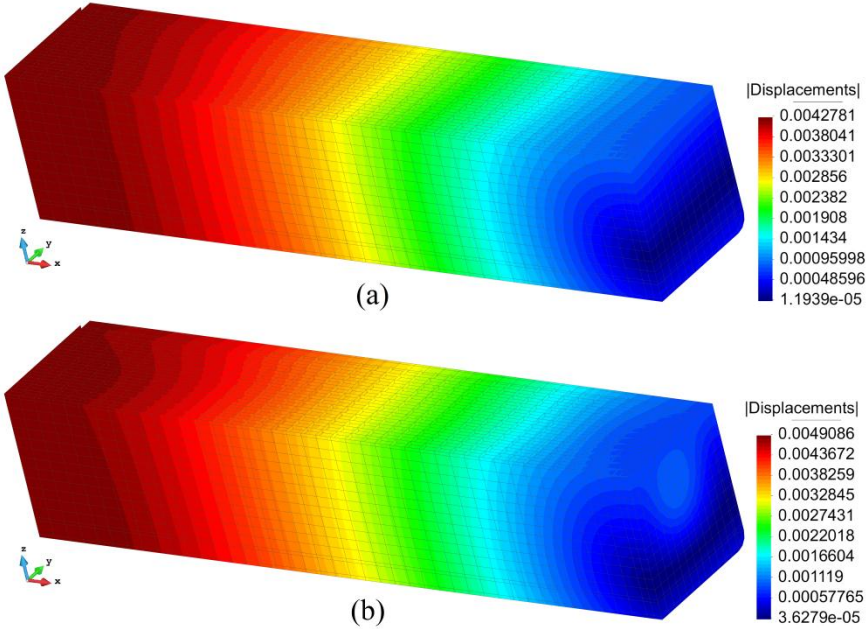


Figure 14 (a) iFEM total displacement [m] distribution for strain data collected from the central deck stiffener, the central girder, and the central longitudinal bulkhead. (b) Direct finite element total displacement [m] distribution.

The error of the maximum displacement produced by the iFEM solution is 12.85% with respect to the FEM maximum displacement. Following to the displacement calculation, the von Mises stresses are computed according to the top surfaces of the shells in both iFEM and direct FEM analysis. Although a large amount of strain-sensor data is not available for this case study, similar to the displacement comparison, von Mises stress distributions are quite coherent when they are compared as shown in Figure 15.

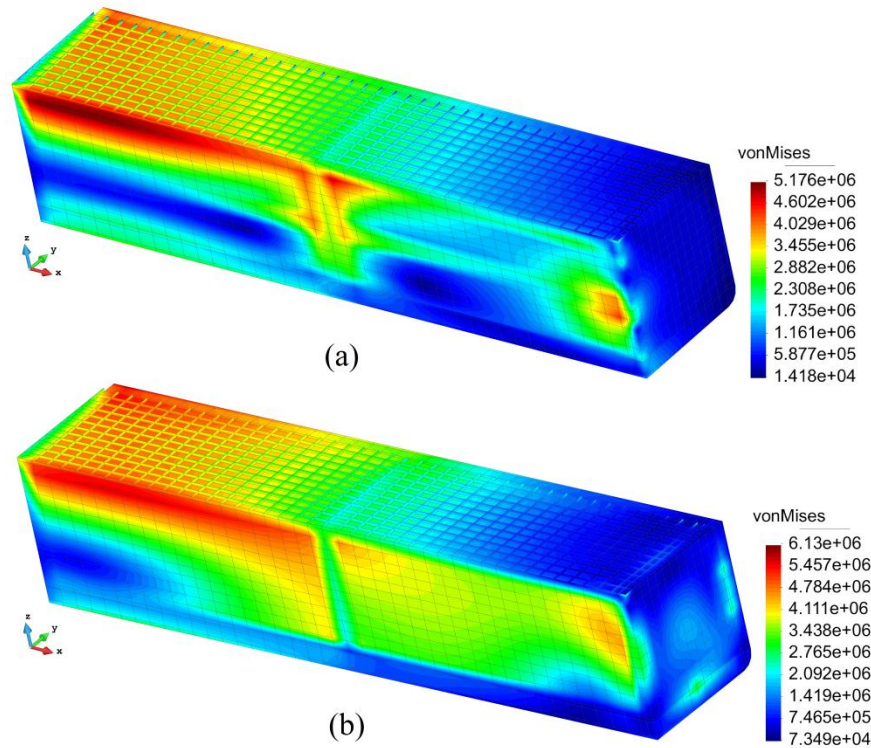


Figure 15 (a) iFEM von Mises stress [Pa] distribution for strain data collected from the central deck stiffener, the central girder, and the central longitudinal bulkhead. (b) Direct finite element vonMises stress [Pa] distribution

The error between the maximum iFEM-reconstructed and direct FEM von Mises stresses is 15.56%. These numerical results have verified that it is still possible to reconstruct sufficiently accurate deformations and von Mises stresses, even if a large amount of strain-sensor data is not available. Consequently, it can be indicated that the iFEM-reconstructed displacement and von Mises stress results are quite precise in terms of practical engineering application. According to results of three case studies, it can be concluded that iFEM methodology is a promising technology for accomplishing accurate displacement and stress monitoring of marine structures.

5. Concluding remarks

Displacement and stress monitoring of a chemical tanker mid-ship section by using iFEM methodology is accomplished in this work. The presented iFEM formulation is based upon the

minimization of weighted-least-squares functional and requires discrete strain data obtained from on-board sensors in order to reconstruct the displacement, strain, and stress fields. In-house hydrodynamic and finite element software are utilized for simulating the on-board strain-sensor data in order to represent a floating structure in real sea environment. First, hydrodynamic loads are obtained and used for the loading condition of a direct FEM analysis of the chemical tanker mid-ship section. Once simulated strain data is obtained from direct FEM analysis, iFEM analysis of three different cases including different number of strain sensors for the same model are examined. The comparisons of the results obtained from both iFEM and direct FEM analyses demonstrate that displacement and stress monitoring of the chemical tanker can be accurately performed based on iFEM methodology. Moreover, the numerical results confirmed that relatively accurate deformed shapes and von Mises stresses can still be reconstructed by exploiting the weighting constants in the least-squares functional of iFEM, even though a large amount of in-situ strain data is absent or only a relatively sparse strain data is collected. Furthermore, it has been observed that using the strain data obtained from strain rosettes located at the central deck stiffener, the central longitudinal bulkhead, and the central girder can be sufficient to reconstruct a precise global deformed shape and von Mises stresses caused by vertical bending moment and shear force due to oscillatory motions. Consequently, it can be indicated that the central deck stiffener, the central longitudinal bulkhead, and the central girder are the optimum locations for placing on-board sensors for a longitudinally framed structure. As a result, it can be concluded that iFEM algorithm is very promising system for performing a precise shape- and stress-sensing of marine structures.

Acknowledgement

The authors would like to acknowledge Dr. Olgun Hizir for his precious guidance during the implementation of the in-house hydrodynamic software.

Appendix A

The derivatives of shape functions \mathbf{B}^m , \mathbf{B}^k , \mathbf{B}^s which are given in Eqs. (1a-b) are defined as

$$\mathbf{B}^m = [\mathbf{B}_1^m \quad \mathbf{B}_2^m \quad \mathbf{B}_3^m \quad \mathbf{B}_4^m] \quad (\text{A.1})$$

$$\mathbf{B}^k = [\mathbf{B}_1^k \quad \mathbf{B}_2^k \quad \mathbf{B}_3^k \quad \mathbf{B}_4^k] \quad (\text{A.2})$$

$$\mathbf{B}^s = [\mathbf{B}_1^s \quad \mathbf{B}_2^s \quad \mathbf{B}_3^s \quad \mathbf{B}_4^s] \quad (\text{A.3})$$

where

$$\left. \begin{aligned} \mathbf{B}_i^m &= \begin{bmatrix} N_{i,x} & 0 & 0 & 0 & 0 & L_{i,x} \\ 0 & N_{i,y} & 0 & 0 & 0 & M_{i,x} \\ N_{i,y} & N_{i,x} & 0 & 0 & 0 & L_{i,y} + M_{i,x} \end{bmatrix} \\ \mathbf{B}_i^k &= \begin{bmatrix} 0 & 0 & 0 & 0 & N_{i,x} & 0 \\ 0 & 0 & 0 & -N_{i,y} & 0 & 0 \\ 0 & 0 & 0 & -N_{i,x} & N_{i,y} & 0 \end{bmatrix} \\ \mathbf{B}_i^s &= \begin{bmatrix} 0 & 0 & N_{i,x} & -L_{i,x} & -M_{i,x} + N_i & 0 \\ 0 & 0 & N_{i,y} & -L_{i,y} - N_i & -M_{i,y} & 0 \end{bmatrix} \end{aligned} \right\} (i=1,2,3,4) \quad (\text{A.4})$$

with the shape functions are given as

$$N_1 = \frac{(1-s)(1-t)}{4} \quad (\text{A.5})$$

$$N_2 = \frac{(1+s)(1-t)}{4} \quad (\text{A.6})$$

$$N_3 = \frac{(1+s)(1+t)}{4} \quad (\text{A.7})$$

$$N_4 = \frac{(1-s)(1+t)}{4} \quad (\text{A.8})$$

$$N_5 = \frac{(1-s^2)(1-t)}{16} \quad (\text{A.9})$$

$$N_6 = \frac{(1+s)(1-t^2)}{16} \quad (\text{A.10})$$

$$N_7 = \frac{(1-s^2)(1+t)}{16} \quad (\text{A.11})$$

$$N_8 = \frac{(1-s)(1-t^2)}{16} \quad (\text{A.12})$$

and

$$L_1 = y_{14}N_8 - y_{21}N_5 \quad (\text{A.13})$$

$$L_2 = y_{21}N_5 - y_{32}N_6 \quad (\text{A.14})$$

$$L_3 = y_{32}N_6 - y_{43}N_7 \quad (\text{A.15})$$

$$L_4 = y_{43}N_7 - y_{14}N_8 \quad (\text{A.16})$$

$$M_1 = x_{41}N_8 - x_{12}N_5 \quad (\text{A.17})$$

$$M_2 = x_{12}N_5 - x_{23}N_6 \quad (\text{A.18})$$

$$M_3 = x_{23}N_6 - x_{34}N_7 \quad (\text{A.19})$$

$$M_4 = x_{34}N_7 - x_{41}N_8 \quad (\text{A.20})$$

Note that x_{ij} and y_{ij} can be expressed in terms of local coordinates of iQS4 element as

$$\left. \begin{aligned} x_{ij} &= x_i - x_j \\ y_{ij} &= y_i - y_j \end{aligned} \right\} (i = 1, 2, 3, 4; j = 1, 2, 3, 4) \quad (\text{A.21})$$

and the parent space coordinates are defined as $s, t \in [-1, +1]$.

Appendix B

Cross-section of the presented barge model is similar to a typical chemical tanker cross-section. Detailed dimensions of structural components in the barge model's cross-section and its isometric view is presented in Figure B1-B2, respectively.

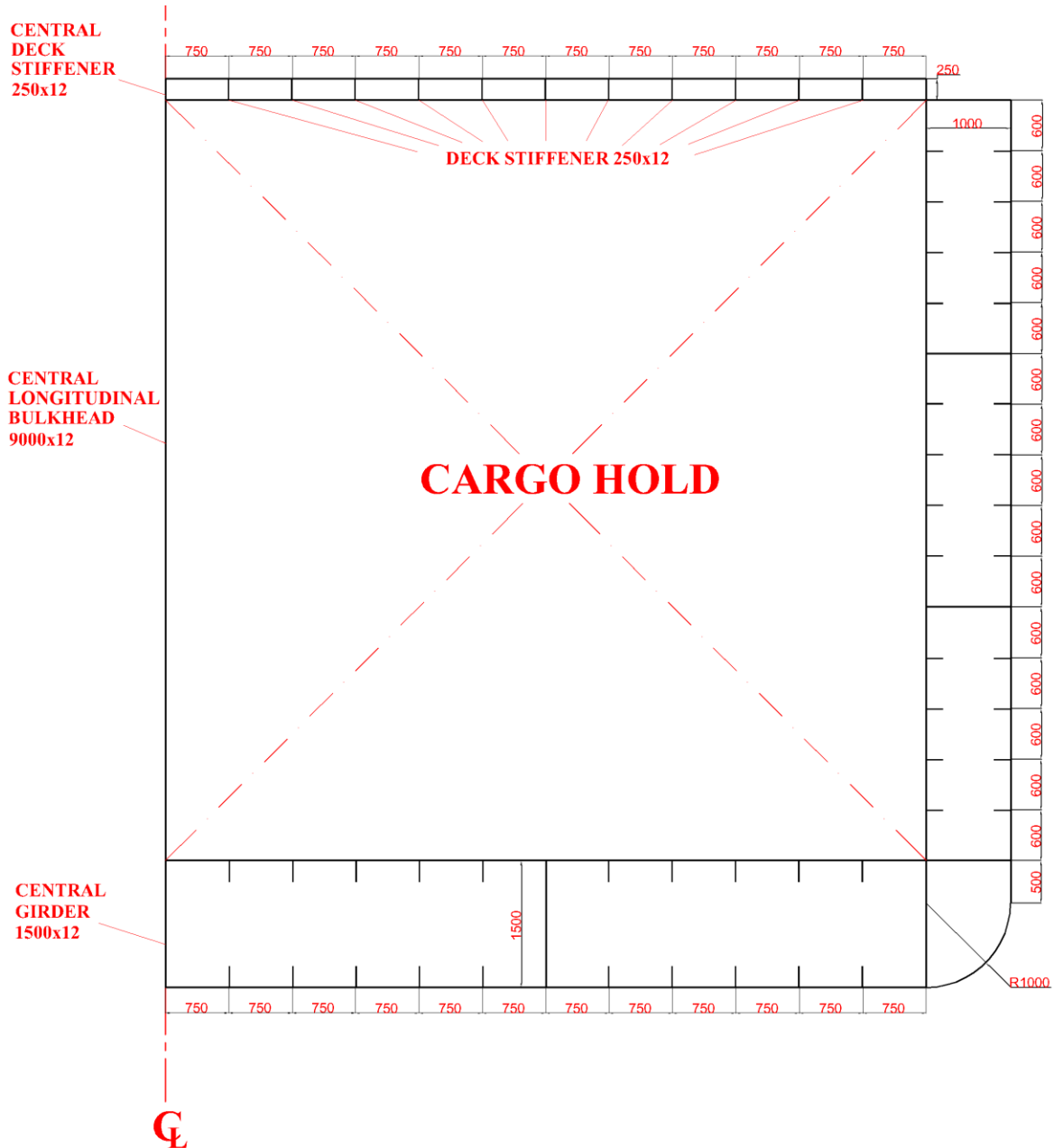


Figure B1 Detailed dimensions [mm] of structural components in half cross-section of the barge

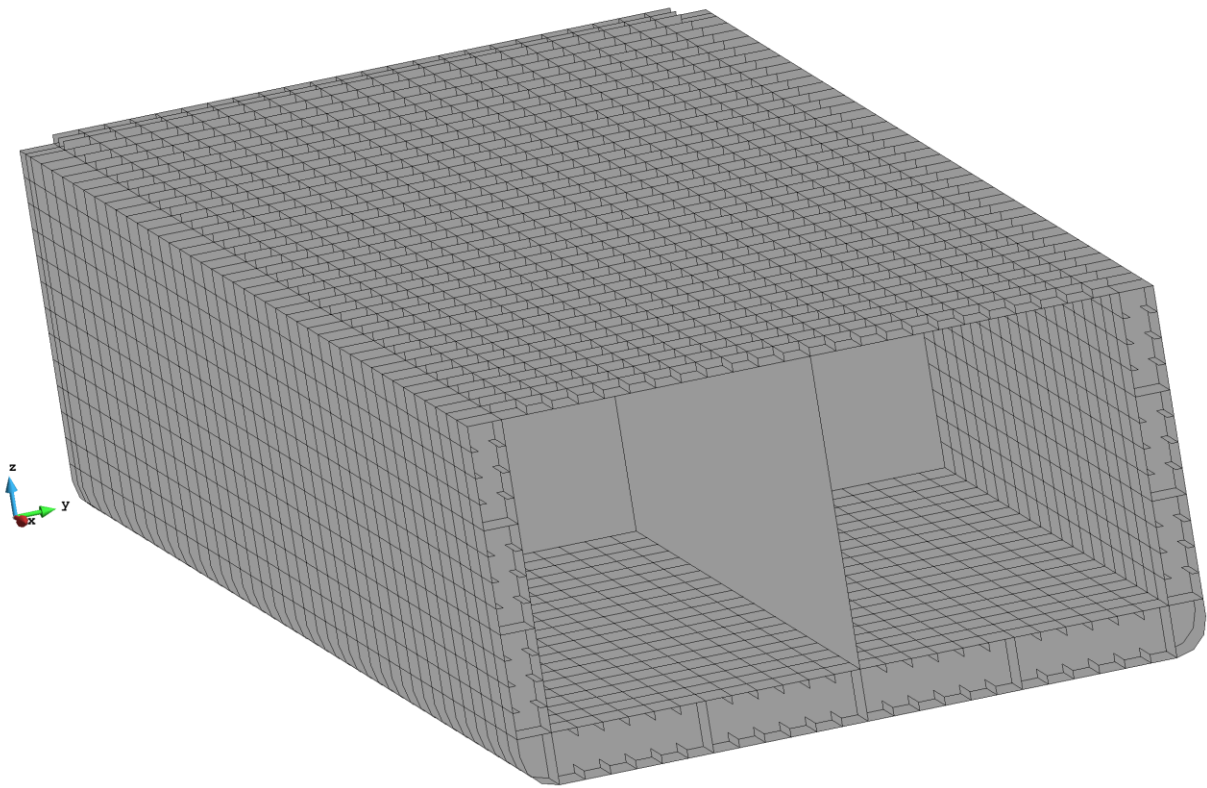


Figure B2 Isometric view of barge cross-section

Appendix C

Several isometric views of the barge structural model are illustrated in Figures C1-C3 in order to show its structural topology. Cargo tanks in the full barge model can be seen in Figure C1. Structural details of the quarter barge model is shown in Figure C2. A detailed view of double side and double bottom framing is presented in Figure C3.

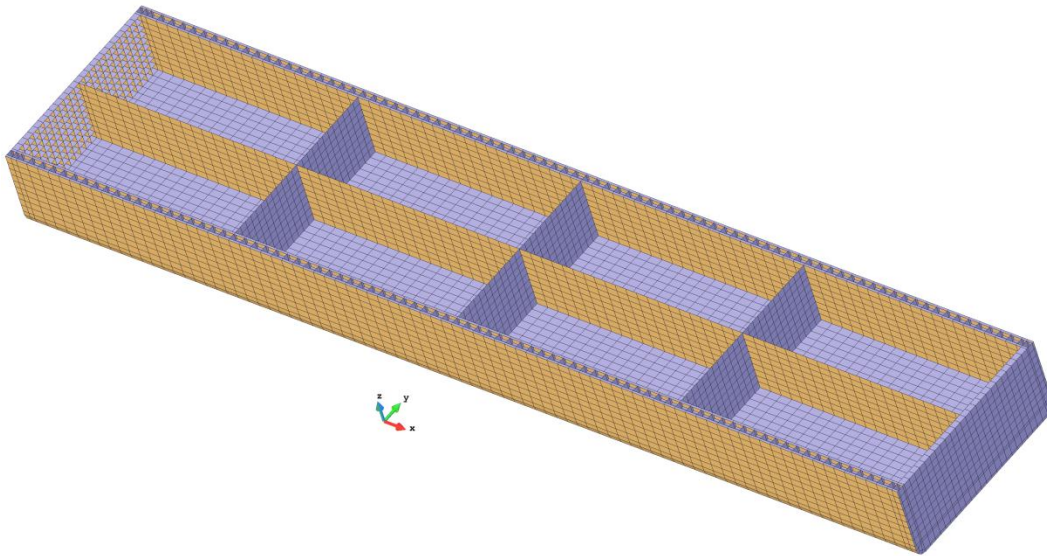


Figure C1 Isometric view of cargo tanks

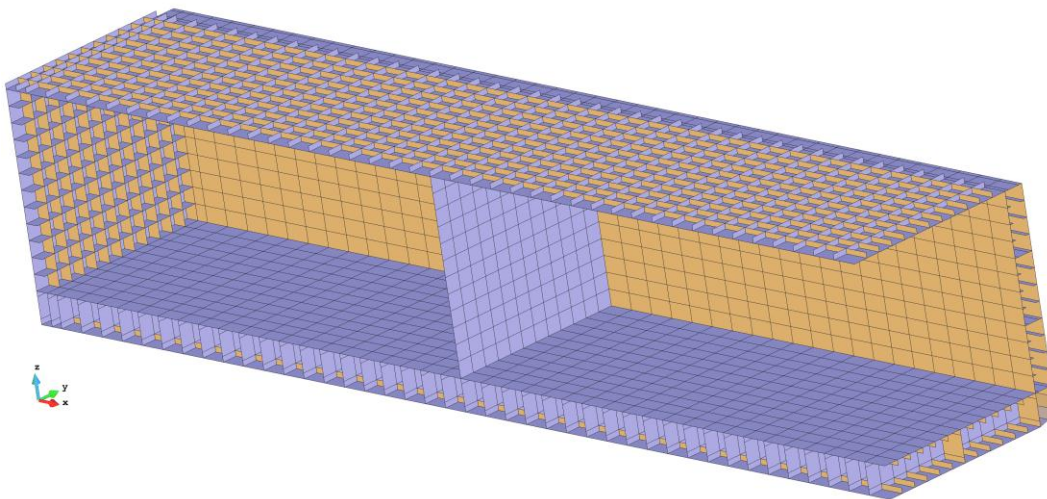


Figure C2 Structural details in the quarter barge model

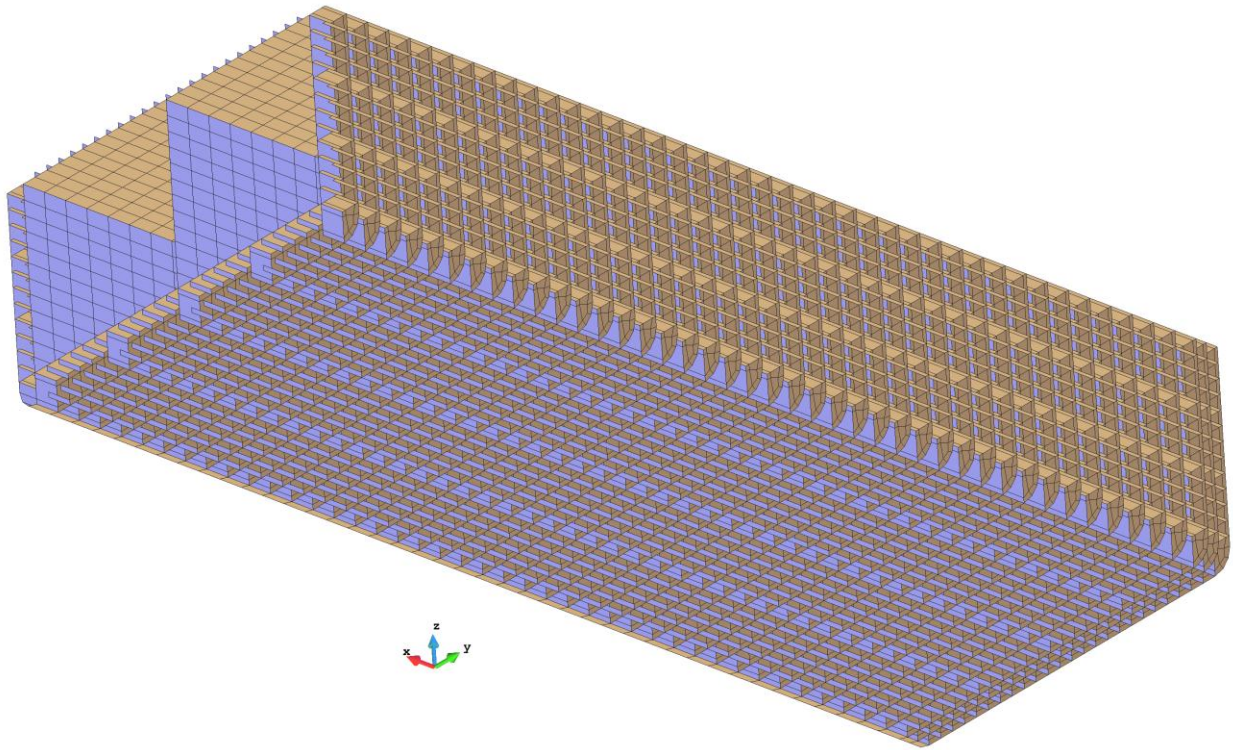


Figure C3 Double side and double bottom framing details

References

- American Bureau of Shipping. (1995). Guide for Hull Condition Monitoring Systems.
- Andersson, S., Haller, K., Hellbratt, S. E., & Hedberg, C. (2011). Damage monitoring of ship FRP during exposure to explosion impacts. In Proc. 18th Inter. Conf. Composite Materials, Jeju Island, Korea.
- Beck, R. F., & Loken, A. E. (1989). Three-dimensional effects in ship relative-motion problems. *Journal of Ship Research*, 33(4), 261-268.
- Bhatti, M. A. (2006). Advanced topics in finite element analysis of structures: with Mathematica and MATLAB computations. John Wiley & Sons, Inc.
- Cerracchio, P., Gherlone, M., Mattone, M., Di Sciuva, M., & Tessler, A. (2010). Shape sensing of three-dimensional frame structures using the inverse finite element method. In: Proceedings of 5th European Workshop on Structural Health Monitoring, Sorrento, Italy.
- Cerracchio, P., Gherlone, M., Di Sciuva, M., & Tessler, A. (2013). Shape and Stress Sensing of Multilayered Composite and Sandwich Structures Using an Inverse Finite Element Method. In: Proceedings of V International Conference on Computational Methods for Coupled Problems in Science and Engineering, Ibiza, Spain.
- Cerracchio, P., Gherlone, M., Di Sciuva, M., & Tessler, A. (2015). A novel approach for displacement and stress monitoring of sandwich structures based on the inverse Finite Element Method. *Composite Structures*, 127, 69-76.
- Cook, R. D. (1994). Four-node 'flat' shell element: drilling degrees of freedom, membrane-bending coupling, warped geometry, and behaviour. *Computers and Structures*, 50(4), 549-555.
- Det Norske Veritas, Hull Monitoring Systems. (2011). DNV Rules for Classification of Ships, Part 6, Chapter 11.
- Dokkum, K. V. (2003). Ship Knowledge, a Modern Encyclopedia. Dokmar: Netherlands.
- Gherlone, M., Cerracchio, P., Mattone, M., Di Sciuva, M., & Tessler, A. (2011). Beam shape sensing using inverse finite element method: theory and experimental validation. In: Proceeding of 8th International Workshop on Structural Health Monitoring, Stanford, CA

- Gherlone, M., Cerracchio, P., Mattone, M., Di Sciuva, M., & Tessler, A. (2012). Shape sensing of 3D frame structures using an inverse Finite Element Method. *International Journal of Solids and Structures*, 49(22), 3100-3112.
- Gherlone, M., Cerracchio, P., Mattone, M., Di Sciuva, M., & Tessler, A. (2014). An inverse Finite Element Method for beam shape sensing: theoretical framework and experimental validation. *Smart Materials and Structures*, 23(4), 045027.
- Hageman, R., Aalbetrs, P., Shaik, M., & Van den Boom, H. (2013). Development of an Advisory Hull Fatigue Monitoring System. In *Proc. SNAME Annual Meeting & Expo & Ship Production Symposium*, Bellevue, WA.
- Lloyds Register. (2004). *ShipRight Ship Event Analysis*.
- Majewska, K., Mieloszyk, M., Ostachowicz, W., & Król, A. (2014). Experimental method of strain/stress measurements on tall sailing ships using Fibre Bragg Grating sensors. *Applied Ocean Research*, 47, 270-283.
- Nichols, J. M., Fackler, P. L., Pacifici, K., Murphy, K. D., & Nichols, J. D. (2014). Reducing fatigue damage for ships in transit through structured decision making. *Marine Structures*, 38, 18-43.
- Papanikolaou, A. D., & Schellin, T. E. (1992). A three-dimensional panel method for motions and loads of ships with forward speed. *Journal of Schifftechnik – Ship Technology Research*, 39 (4), 147-156.
- Phelps, B., & Morris, B. (2013). *Review of Hull Structural Monitoring Systems for Navy Ships* (No. DSTO-TR-2818). Defense Science and Technology Organization Victoria (Australia) Maritime Platforms Div.
- Quach, C.C., Vazquez, S.L., Tessler, A., Moore, J.P., Cooper, E.G., & Spangler, J.L. (2005). Structural anomaly detection using fiber optic sensors and inverse finite element method. In: *Proceedings of AIAA Guidance, Navigation, and Control Conference and Exhibit*, San Francisco, California.
- Sielski, R. A. (2012). Ship structural health monitoring research at the Office of Naval Research. *JOM*, 64(7), 823-827.

- Tessler, A., & Hughes, T. J. (1983). An improved treatment of transverse shear in the Mindlin-type four-node quadrilateral element. *Computer Methods in Applied Mechanics and Engineering*, 39(3), 311-335.
- Tessler, A., & Spangler, J.L. (2003). A variational principle for reconstruction of elastic deformation of shear deformable plates and shells, NASA TM-2003-212445.
- Tessler, A., & Spangler, J.L. (2004). Inverse FEM for full-field reconstruction of elastic deformations in shear deformable plates and shells. In: *Proceedings of 2nd European Work-shop on Structural Health Monitoring*, Munich, Germany.
- Tessler, A., & Spangler, J. L. (2005). A least-squares variational method for full-field reconstruction of elastic deformations in shear-deformable plates and shells. *Computer Methods in Applied Mechanics and Engineering*, 194(2), 327-339.
- Tessler, A., Di Sciuva, M., & Gherlone, M. (2009). A refined zigzag beam theory for composite and sandwich beams. *Journal of Composite Materials*, 43, 1051–1081.
- Tessler, A., Di Sciuva, M., & Gherlone, M. (2010). A consistent refinement of first-order shear deformation theory for laminated composite and sandwich plates using improved zigzag kinematics. *Journal of Mechanics of Materials and Structures*, 5(2), 341-367.
- Tessler, A., Spangler, J. L., Gherlone, M., Mattone, M., & Di Sciuva, M. (2011). Real-Time characterization of aerospace structures using on-board strain measurement technologies and inverse finite element method. In: *Proceedings of the 8th International Workshop on Structural Health Monitoring*, Stanford, CA.
- Tessler, A., Spangler, J. L., Gherlone M., Mattone M., & Di Sciuva, M. (2012). Deformed shape and stress reconstruction in plate and shell structures undergoing large displacements: application of inverse finite element method using fiber bragg grating strains. In: *Proceedings of 10th World Congress on Computational Mechanics*, Sao Paulo, Brazil.
- Torkildsen, H. E., Grovlen, A., Skaugen, A., Wang, G., Jensen, A. E., Pran, K., & Sagvolden, G. (2005). Development and applications of full-scale ship hull health monitoring systems for the Royal Norwegian Navy. Norwegian Defence Research Establishment Kjeller.

Van der Cammen, J. J. (2008). Fatigue prediction and response monitoring on a FPSO. TU Delft, Delft University of Technology.

Vazquez, S.L., Tessler, A., Quach, C.C., Cooper, E.G., Parks, J., & Spangler J.L. (2005). Structural health monitoring using high-density fiber optic strain sensor and inverse finite element methods, NASA TM-2005-213761.

Wehausen, J. V., & Laitone, E. V. (1960). Surface waves (pp. 446-778). Springer Berlin Heidelberg.

Zhu, B., & Frangopol, D. M. (2013). Incorporation of structural health monitoring data on load effects in the reliability and redundancy assessment of ship cross-sections using Bayesian updating. *Structural Health Monitoring*, 12(4), 377-392.